An investigation of recycled rubber composites reinforced with micro glass bubbles: An experimental and numerical approach

Gamze Cakir Kabakci[1,2], Emin Bayraktar[2], Ozgur Aslan[1,3]*

[1]Department of Mechanical Engineering, Atilim University,06830, Ankara, Turkey
[2]School of Mechanical and Manufacturing Engineering, ISAE-Supmeca-Paris, Saint Ouen, 93407 Paris, France
[3]Department of Engineering Science, University of Oxford, Oxford OX1 3PJ, UK
*Correspondence: ozgur.aslan@eng.ox.ac.uk; Tel.: +44 7879 710892

Abstract: Recycled rubber is extensively used as recyclable material favored for its lightweight properties and cost-effectiveness, but it often suffers from low mechanical strength, limiting its broader application. This study aims to enhance mechanical properties of devulcanized recycled rubber by incorporating micro glass bubble (GB) reinforcements characterized by a density of 0.65 g/cm³ and a modulus of elasticity of 3.5 GPa, that offers excellent weight reduction with its high strength-to-density ratio. Uniaxial compression tests are performed on samples with varying GB volume fractions of 5%, 10%, and 15%. The results are numerically validated using finite element analysis (FEA) in ABAQUS/Standard, considering varying degrees of inclusion randomization. A 2D representative volume element (RVE) is modeled with randomly distributed GBs and subjected to periodic boundary conditions (PBCs) to replace heterogeneous composite with an equivalent homogeneous material. Numerical analyses are conducted for GBs with different diameters (30, 40, and 50 μm), revealing minimal influence on the results. The stress-strain behavior of random heterogeneous composite is described by analyzing average stress and strain tensors across integration volume elements. Afterwards, the RVE with a length of 238 μm is anticipated to demonstrate the most effective adjustment to the macroscale response. To illustrate the effect of different glass bubble diameters, numerical analyses are also carried out for the expected RVE size with 30, 40, and 50 μm diameters. Inclusions varying in diameter from 20 to 50 μm and 10 to 60 μm are also simulated. Notably, variations in the sizes of inclusions seem to have minimal impact on the numerical results. The comparison between experimental and numerical results demonstrate high accuracy of the numerical simulations, confirming the developed method successfully predicts the behavior of composite material.

Keywords: recycled rubber composite; glass bubble; homogenization; representative volume element; periodic boundary condition

1. Introduction

Industries like aeronautics, automotive, and transportation extensively use recycled rubber (RR) for various applications that demand attributes like high toughness, excellent impact resistance, cost-effectiveness, and lightweight structures. Rubber waste is gathered and categorized as industrial waste in numerous sectors, such as automotive and aerospace. Around 5-15% of the total output is attributed to these wastes [1,2]. In traditional rubber manufacturing, there are a few instances where scrap rubber is produced. However, recovering energy from scrap rubber is detrimental to the environment, exacerbating ecological harm through

emissions and waste [3]. The lack of utilization of these RRs is also regarded as a financial loss, further underscoring the necessity for recycling [2,4]. Thus, it is crucial to develop cost-effective techniques for recycling waste rubber.

The recycling process for rubber begins with the collection of industrial rubber scraps generated from manufacturing activities, such as tire production and automotive components. These scraps are then ground into smaller particles, increasing their surface area and preparing them for further treatment. Next, the ground rubber undergoes thermomechanical devulcanization, which involves applying heat and mechanical energy to break sulfur cross-links that bind the rubber. This process restores the rubber's plasticity, transforming it into reclaimed rubber [2,5]. Finally, the reclaimed rubber is revulcanized by mixing it with new sulfur and additives, re-establishing the desired cross-linking structure and enhancing its properties for reuse in new products. A schematic drawing illustrating rubber recycling process is presented in Figure 1.

Figure 1. Schematic drawing of rubber recycling

Once rubber undergoes crosslinking, recycling becomes challenging. However, the devulcanization process enables the reversal of crosslinking in cured rubber [2,4]. This results in acquiring recycled material with characteristics similar to original material [6,7]. Devulcanized rubber improves interaction and adherence with the matrix [8]. Compared to other materials, rubber can withstand significant elastic deformation under stress, and upon unloading, it can revert to initial shape without undergoing permanent deformation. On the other hand, devulcanized rubber often fails to return to original shape following a substantial

deformation [9] and it has relatively low stiffness and strength [10]. To improve these properties, it is necessary to reinforce the matrix by stronger and stiffer microscale particles [11, 12].

Various fillers require different properties for an ideal reinforcement, based on the type of inclusion used. To enhance the reinforcement of rubber particles, various micro- and nanoscale fillers are employed [13-15]. Existing research on recycled rubber composites suggests that incorporating fillers enhances the physical and mechanical properties [16-18]. Moreover, it results in the production of cost-effective and lightweight composites suitable for diverse application areas.

Recent advancements in the field of recycled rubber composites have demonstrated significant improvements through the integration of microscale and nanoscale reinforcements. Studies such as Kabakci et al. have focused on toughening mechanisms in composites by utilizing glass bubbles, alumina fibers, and other fillers [19]. Further research by Sun et al. emphasizes the role of hollow glass microspheres in enhancing both tensile strength and energy absorption properties of polymer composites [2,21]. Additionally, Ma et al. explored covalent bonding techniques in nanocomposites, further enhancing mechanical properties and energy storage capabilities in rubber-based systems [22].

The use of recycled EPDM in development of the composites reinforced with alumina fiber, as investigated by Irez et al. [13], exhibits a significant advancement in the creation of cost-effective and lightweight materials. Dhingra et al. [16] further expanded the scope by examining the properties of alumina fibers, shedding light on its potential applications and variability in the creation of lightweight composites. Geim and Novoselov's work on graphene [22] has provided lightweight yet strong composite materials. In the field of polymer science, Platzer's investigation into the fracture mechanics of polymers [24] provides fundamental insights crucial for the development of lightweight composite materials. Additionally, Zhang and Lei's work [25] offers an innovative approach for achieving cost-effective lightweight materials, particularly in applications like chemical mechanical polishing on glass substrates. Furthermore, the study by Zhang et al. [26] explores the functionalization of graphene nanoplatelets in silicone rubber composites, demonstrating a promising pathway for cost-effective improvements in mechanical and thermal properties. Together, these research efforts highlight diverse strategies in the development of cost-effective and lightweight composites, incorporating recycling, creative material selections, and advanced manufacturing methods.

Glass bubbles, or hollow glass microspheres (GBs), offer a substitute for the conventional inorganic fillers in reinforced rubber composites across different applications [27,19]. Their high strength-to-density ratio makes them well-suited for demanding polymer processing operations in various contexts. GBs, characterized by an ideal spherical shape and an aspect ratio of one, function as excellent volume fillers, providing notable advantages such as weight reduction, improved performance, and enhanced processing [28]. Kabakci, Aslan, and Bayraktar [1] conducted a comprehensive review on the analysis of reinforced RR composites, emphasizing the role of GBs. Râpa et al.'s study [29] explores the effect of GBs on the properties of post-consumer recycled polypropylene, revealing their positive impact on material characteristics. This work underscores the potential of GBs in improving the overall performance of recycled composites. Kabakci, Aslan, and Bayraktar [30] delve into the toughening mechanisms of RR based composites including GBs, GFs, and AFs. GBs contribute to the unique characteristics of these composites, influencing toughness and overall material behavior. K-Çakır et al. [31,32] focus on the toughening mechanism and numerical modeling of RR composites with GFs and AFs. These studies further highlight the significance of GBs

in achieving desirable properties in composite materials. In summary, glass bubbles play a crucial role in reinforced rubber composites, offering a range of beneficial properties. These studies collectively underscore the impact of GBs on weight reduction, improved performance, and enhanced processing, showcasing their importance in advancing composite material properties.

In heterogeneous structures, the effective physical behavior is heavily influenced by geometry, properties, and distribution of inclusions. However, conducting simple experimental observations on multiple specimens with varying phase characteristics and volume fractions is often impractical due to time and cost constraints [33]. To address this challenge, various homogenization approaches have been developed, aiming to develop constitutive models applicable at the macroscopic scale, utilizing an approach that incorporates averaging and homogenization.

Among these analytical approaches, micromechanical models, including the Halpin-Tsai (H-T) model [34] and the Mori-Tanaka model [35], estimate the elastic properties of composites by considering factors like geometry and elastic properties of both inclusions and matrix. The H-T model averages properties of components to derive overall property and is suitable for linear material properties, such as elastic moduli [34,36]. This method only accounts for one microstructural factor: the proportion of volume occupied by heterogeneities. Equivalent material properties are determined analytically by solving a boundary value problem (BVP) using models like Eshelby's [37], Hashin's [38], Hashin and Shtrikman's [39], and Hill's [40], all of which employ self-consistent approaches.

Additionally, asymptotic expansion theory, formulated by Sanchez-Palencia [41] and Bensoussan, Lions, Papanicolaou [42], offers another mathematical approach to derive effective overall properties and local stresses and strains for microscopic geometries. Studies on the macroscopic linear properties have also been conducted by Beran [43], and Torquato [44], while random distributions of heterogeneity have been explored by Milton [45], Besson et al. [46], Kroner [47], Sanchez-Palencia and Zaoui [48] and Nemat-Nasser [49].

In terms of computational homogenization, behavior of heterogeneous materials is governed by constitutive laws and spatial distribution of constituents. Numerous research on numerical homogenization approaches exist in literature. Suquet [50], [51] employed an averaging approach to address non-linear problems across two scales. Following the application of deformation gradient tensor at the microscopic level, an averaging formulation is employed to calculate the macroscopic stress tensor [2]. The concept of the Representative Volume Element (RVE), introduced by Hill [52], represents a sufficiently large volume of heterogeneous material that statistically reflects the composite. The finite element method is commonly used to analyze the RVE level, as demonstrated by Terada and Kikuchi [53], Smit [54], Smit et al. [55], Miehe et al. [56], Feyel and Chaboche [57]. The work of Moulinec [58] and Miehe [59], [60] extended this approach to include large deformations characterized by nonlinear material behavior, without any predefined microstructural patterns. Geers and Kouznetsova [61–63] advanced second-order homogenization techniques, solving BVPs at the microscale employing the deformation gradient tensor along with the associated Lagrangian gradient [64].

In this study, cost-effective rubber-based (RR) composites are designed with glass bubble (GB) reinforcements to enhance mechanical properties of RR across various volume fractions. After determining the inclusions in the matrix, the composites undergo compression tests to obtain their stress-strain curves. The performance of H-T model, as a rule of mixture, is then evaluated to predict the homogenized moduli of the composite materials. Additionally, the uniaxial response of the composites is analyzed using macromechanical finite element simulations in

ABAQUS/Standard. For the homogenization process, a 2D RVE with randomly distributed spherical GBs is used. The RVE size is set based on the length of a side of the square domain, corresponding to a specific number of inclusions and a defined volume fraction. The determination of isotropic elastic properties is achieved by enforcing periodic boundary conditions (PBCs) on the RVE. To characterize the stress-strain response, average strain and stress tensors across integration volume elements are subsequently calculated.

By drawing comparisons with other studies in the literature, it is demonstrated that the inclusion of GBs offers a robust solution for enhancing recycled rubber composites. At the same time, areas where the findings diverge from the established literature are highlighted, providing insights into the unique behavior of devulcanized recycled rubber composites. While significant progress has been made in reinforcing recycled rubber, there is a notable lack of research on the use of micro glass bubbles as reinforcements. This study addresses this gap by combining experimental data with numerical simulation techniques, particularly finite element analysis using representative volume elements (RVE). The novelty lies in this dual approach, which offers a more comprehensive understanding of the material's behavior compared to prior studies that focus solely on experimental results.

To provide a clear overview of the entire research process, a flowchart is presented in Figure 2, which outlines the key stages of the study, including material selection, composite manufacturing, experimental testing, numerical analysis using finite element analysis (FEA), and the comparison of experimental and numerical results. This comprehensive visual summary facilitates the understanding of the methodology and the sequential flow of the study's key steps.

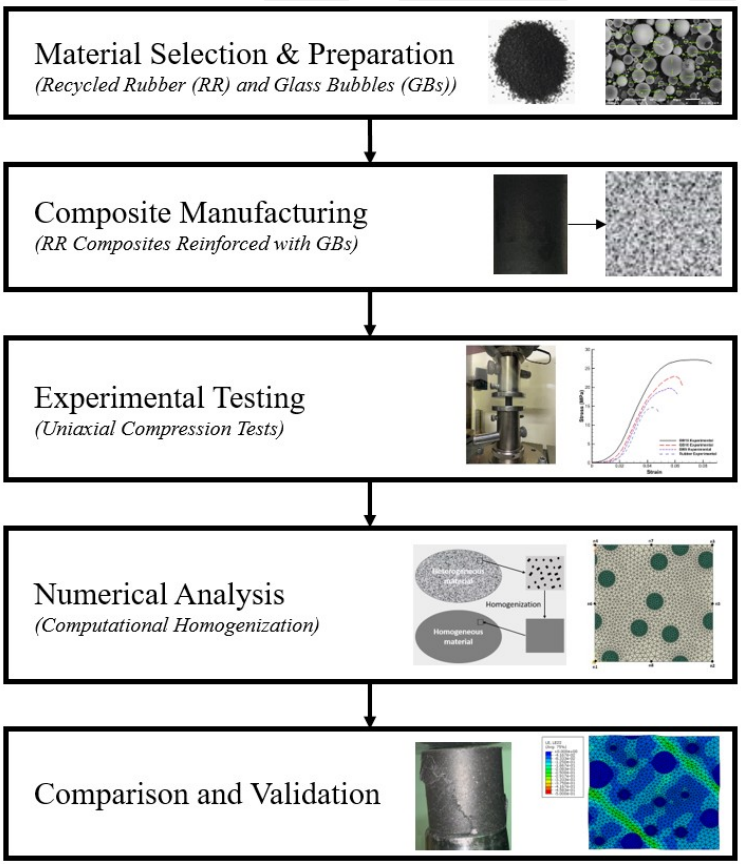

Figure 2. Flowchart for the research methodology of RR composites

reinforced with GBs

2. Experimental Methods

The recycled rubber employed in this study has been sourced from manufacturers of sports equipment, obtained as fresh scrap obtained from manufacturing line. Notably, this recycled rubber does not include any metallic inclusions. The rubber particles have an average diameter of 50 µm, a density of 1.51 g/cm³, and a modulus of elasticity of 10 MPa. Additionally, GBs are manufactured by 3M™ Glass Bubbles K1 [28] and they exhibit a density of 0.65 g/cm³, a diameter of 30 µm, and an elasticity modulus of 3546 MPa [2]. Figure 3 shows SEM images illustrating GB reinforcements employed in the current study.

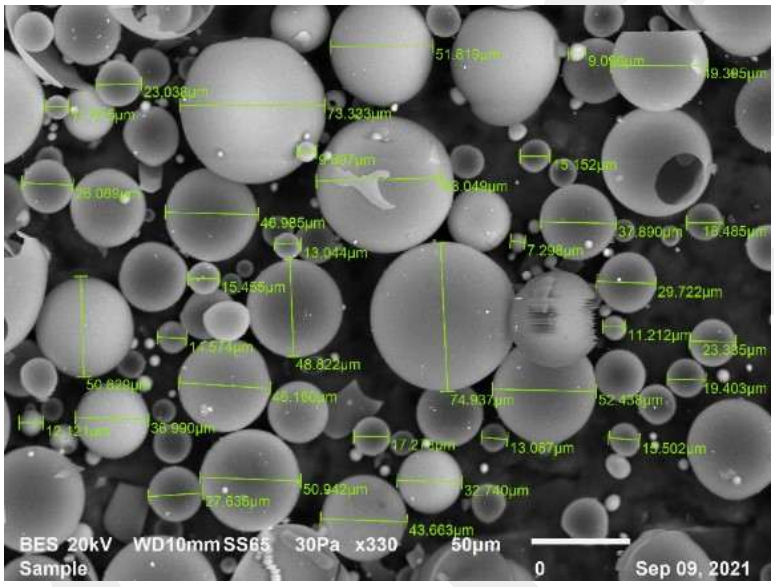

Figure 3. SEM image of GBs

ISAE-Supmeca-Paris, School of Mechanical and Manufacturing Engineering - Quartz Laboratory

Moreover, epoxy resin serves as a binding agent between RR and GBs. The degree of cross-linking significantly influences the mechanical properties [13], [19]. Improving the toughness of the composites can enlarge the plastic zone in the structure, enabling the material to dissipate additional fracture energy. Consequently, the composite material mixture is composed of 95 weight percent (wt. %) RR and 5 wt. % epoxy. Pure dry epoxy resin, produced by Yantai Yuanli Machinery Manufacturing Co. of the Chinese Society, is available as High Purity Solid Epoxy Resin. Achieving effective bonding between the inclusions and matrix is crucial during the manufacturing process. However, RRs, due to prior vulcanization processes, lack the free chains necessary to establish new bonds with epoxy resin. RR mixed with epoxy resin is heated in a microwave oven for 4 minutes at 900 W to initiate the devulcanization process. This method aims to break sulfur bonds, facilitating the formation of partially new links, which enhances the flow properties of the recycled rubber and improves its interaction with other materials [32].

Rubber powder is stored in oven at 30-40°C for 72 hours prior to testing to ensure proper preparation. After blending, RR particles are blended with GBs with different volume fractions of 5%, 10% and 15% and milled for 4 hours with Zn-Stearate to ensure uniform distribution. After mixing and achieving a homogeneous composite, the material is left for one day to avoid

any humidity interference. Then, the composites are manufactured through hot compaction, which is carried out at 220◦ C under a pressure of 70 MPa, with a cycle of 20 minutes of heating and 20 minutes of cooling. The hot compaction process is illustrated in Figure 4. Furthermore, specimens are prepared with a diameter of 50 mm and thickness of 9 mm.

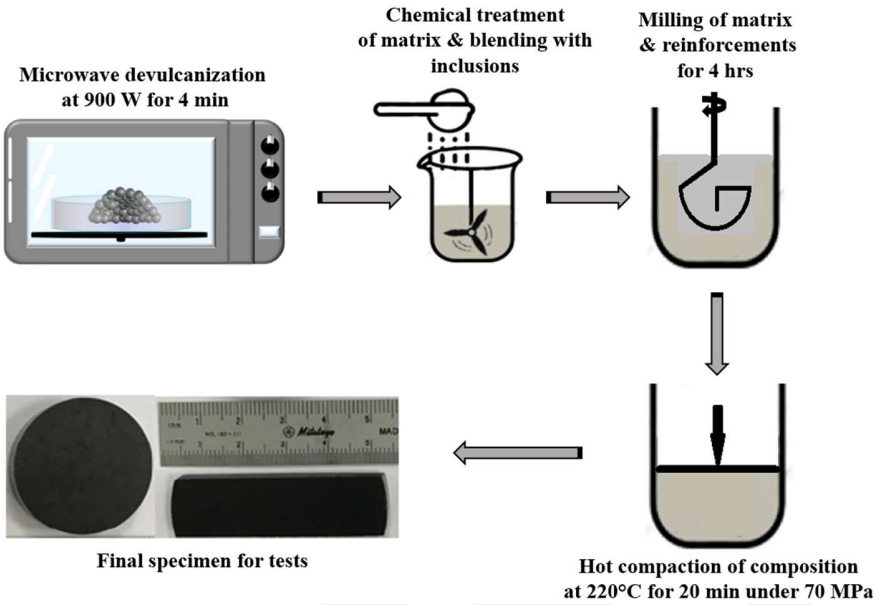

Figure 4. Manufacturing steps of RR-based composites

To describe mechanical properties of composites, they undergo uniaxial compression tests following DIN 50106 standards and with 1 mm/min crosshead speed. Figure 5 illustrates the test setup.

Figure 5. Uniaxial compression test setup

3. Experimental Results

The chemical compositions and the densities of various RR composites manufactured with GB reinforcements are given in the Table 1. In this table, the material density is calculated by considering the contributions of both the matrix (rubber and epoxy) and the glass bubbles. The matrix composition, based on its weight percentages, is converted into volume fractions using the known densities of rubber and epoxy. Similarly, the volumetric content of the glass bubbles is determined based on their proportion in the composite. The overall composite density is then derived by combining the density of the matrix and the glass bubbles, weighted by their respective volume fractions. This method ensures that the final composite density accurately reflects the contributions of both the matrix and the filler. As shown in Table 1, an increase in the amount of GB leads to a reduction in the material's density, making it lighter.

Table 1. Chemical compositions and densities of RR composites [2]

Composite Name	Matrix (vol. %) (Rubber/Epoxy)[1]	Glass Bubble (vol. %)	Density (g/cm3)
GB5	95 (95/5)	5	1.44
GB10	90 (95/5)	10	1.39
GB15	85 (95/5)	15	1.35

[1]Rubber and epoxy in the matrix in wt. %.

To assess the mechanical performance of RR and RR composites reinforced with glass bubbles (GBs), uniaxial compression tests are carried out at a crosshead speed of 1 mm/min. The stress-strain responses for RR and the composite are presented in Figure 6. As seen in the figure, the composite demonstrates higher strength compared to pure rubber, with the addition of reinforcements enhancing the material properties. The uniaxial compression tests demosnstrate that incorporating GBs into the devulcanized recycled rubber matrix significantly enhanced its mechanical properties. This is consistent with findings by Kabakci et al. [6] and Sun et al. [21], who reported similar improvements in the fracture toughness and strength of rubber-based composites reinforced with GBs. The comparison of compression test results, illustrating the impact of incorporating inclusions, is detailed in Table 2. The elastic modulus is typically calculated from the initial linear portion of stress-strain curve, which corresponds to the elastic region where the material deforms reversibly under load. From uniaxial compressive responses, the elastic modulus is computed within the initial strain range where the stress-strain relationship is linear-likely in the strain range of 0.0 to around 0.035, before any yielding occurs. The elastic modulus for the materials in Table 2 are determined by taking the slope of curve in this linear elastic region for each material (GB5, GB10, GB15, and the rubber). The strain range used for calculating the modulus is typically confined to the region before significant plastic deformation occurs.

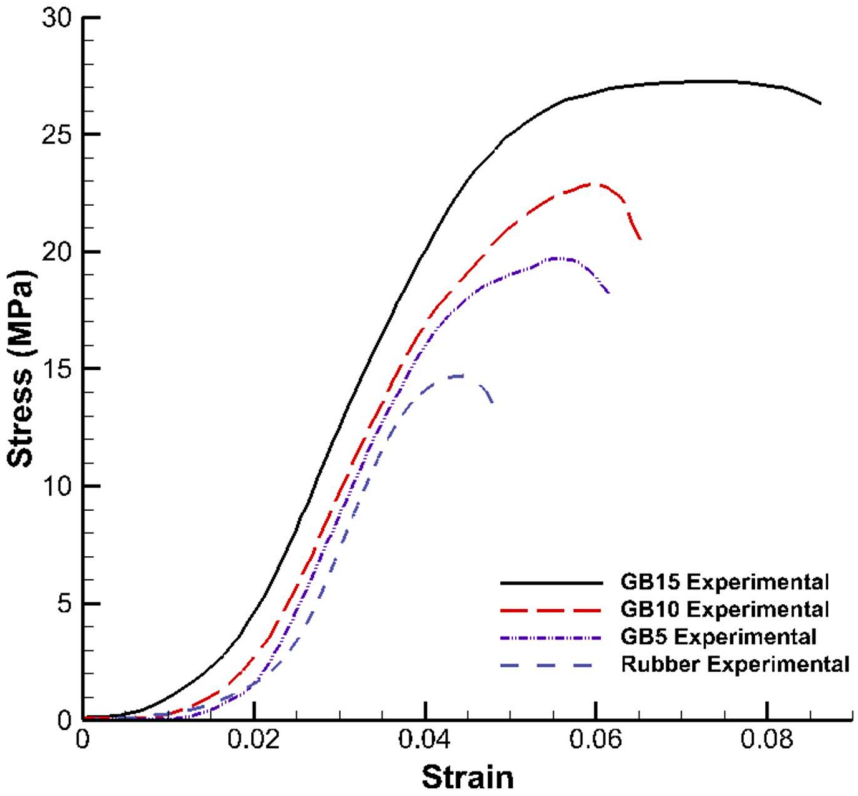

Figure 6. Uniaxial compressive responses of RR and GB composites

Table 2. Comparison of the compression test results

Composite Name	Ultimate Stress, σ_u (MPa)	Strain at Break, ϵ_f (%)	Fracture Stress, σ_f (MPa)	Modulus of Elasticity, E (MPa)
Matrix	14.74	4.80	13.48	323
GB5	19.72	6.16	18.16	367
GB10	22.88	6.53	20.44	424
GB15	27.27	8.64	26.30	512

The test parameters for this study are determined relying on a combination of established literature and prior experience. The glass bubble (GB) volume fractions (5%, 10%, and 15%) are selected in alignment with values commonly reported in the literature for similar composites, as shown in studies like those by Kabakci et al. [30], where these fractions are found to achieve optimal mechanical properties. Additionally, the sizes of the glass bubbles (30, 40, and 50 μm) are chosen based on experience, indicating these sizes to be effective in balancing weight reduction with mechanical reinforcement. Moreover, the uniaxial compression testing conditions are informed by prior experimental setups, where similar parameters are successfully applied to produce reliable and reproducible results.

4. Micromechanical Models

4.1. Analytical Homogenization and Results

Here, we employ a modified Halpin-Tsai (H-T) model for predicting elastic properties of composites. The effect of macro inclusions is given as follows

$$E_c = \left[\frac{3}{8}\frac{1+\xi_f\eta_L V_f}{1-\eta_L V_f} + \frac{5}{8}\frac{1+2\eta_T V_f}{1-\eta_T V_f}\right] E_m, \eta_L = \left[\frac{\frac{E_f}{E_m}-1}{\frac{E_f}{E_m}+\xi_f}\right], \eta_T = \left[\frac{\frac{E_f}{E_m}-1}{\frac{E_f}{E_m}+2}\right], \xi_f = 2\frac{L_f}{D_f} \quad (1)$$

in which L and T are longitudinal and transversal moduli. Then, E_C , E_m and E_f are the elasticity moduli of composite, matrix and fiber; V_f, D_f, L_f, and ξ_f are volume fraction, diameter, length, and shape factor of each fiber, respectively [2].

To accurately execute the modified H-T model, a two-step process is necessary. Initially, the modulus of elasticity of the matrix is computed as

$$E_{C1} = \left[\frac{3}{8}\frac{1+\xi_R\eta_L V_R}{1-\eta_L V_R} + \frac{5}{8}\frac{1+2\eta_T V_R}{1-\eta_T V_R}\right] E_E, \eta_L = \left[\frac{\frac{E_R}{E_E}-1}{\frac{E_R}{E_E}+\xi_R}\right], \eta_T = \left[\frac{\frac{E_R}{E_E}-1}{\frac{E_R}{E_E}+2}\right], \xi_R = 2\frac{L_R}{D_R} \quad (2)$$

where E_{C1}, E_R and E_E the elasticity moduli of matrix, devulcanized rubber, and epoxy; V_R, D_R, L_R, and ξ_R are the volume fraction, diameter, length, and the shape factor of rubber particles, respectively [2]. By adding the glass bubble

$$E_C = \left[\frac{3}{8}\frac{1+\xi_G\eta_L V_G}{1-\eta_L V_G} + \frac{5}{8}\frac{1+2\eta_T V_G}{1-\eta_T V_G}\right] E_{C1}, \eta_L = \left[\frac{\frac{E_G}{E_{C1}}-1}{\frac{E_G}{E_{C1}}+\xi_G}\right], \eta_T = \left[\frac{\frac{E_G}{E_{C1}}-1}{\frac{E_G}{E_{C1}}+2}\right], \xi_R = 2\frac{L_G}{D_G} \quad (3)$$

in which E_C and E_G are the elastic moduli of final composite and GBs; V_G, D_G, L_G, and ξ_G are the volume fraction, diameter, length, and the shape factor of GB particles, respectively. This process is conducted for all composites and Table 3 presents the homogenized elastic moduli alongside the experimental values for comparison.

Table 3. Analytical and experimental elastic moduli [2]

Composite Name	H-T Modulus, E_c (MPa)	Experimental Modulus, E (MPa)
GB5	231	367
GB10	259	456
GB15	293	570

However, the elastic moduli obtained by experimentally and by H-T model do not demonstrate satisfactory agreement. Despite this disparity, there is a consistent trend in the variation of elastic moduli, where values consistently increase with the introduction of GBs into the matrix. The discrepancy in stiffness values may stem from the analytical model's inherent limitation,

as it solely predicts composite elasticity based on factors such as geometry and volume fraction of the heterogeneity, elastic properties of both inclusions and matrix, and an average of individual component properties to derive overall material property. To improve the predictive accuracy of the analytical model, introducing refinements is crucial. One key refinement involves incorporating more complex factors that better represent the real structure. Specifically, accounting for non-uniform particle distribution and realistic particle shapes can significantly improve the model's precision.

4.2. Computational Homogenization and Results

Analytical models face challenges when applied to intricate problems, and their precision may be insufficient for composite materials. Consequently, numerical approaches, capable of providing results with enhanced accuracy, are used to analyze material property. By leveraging numerical simulations, the study aims to address the constraints of analytical methods and offer a more precise understanding of how the composite material behaves under varying conditions, particularly when incorporating glass bubble particles.

The uniaxial behavior of composites, along with the impact of fillers on the finite strain response, are investigated with macromechanical finite element (FE) simulations by ABAQUS/Standard. A 2D FE model, corresponding to the dimensions of the test specimen, is utilized to replicate the stress-strain response of the composite. Simulations of uniaxial compression tests are performed for GB5, GB10, and GB15 configurations, where the macrostructure is defined as a matrix embedded with randomized microspherical particles of 30 μm in diameter. A Python script is employed to randomize the distribution of GBs within matrix geometry, streamlining model creation process in ABAQUS/CAE.

Initially, a microsphere is created within the rectangle that represents the matrix by implementing a "random" function in the script. Subsequently, an algorithm is formulated to ensure no two circles overlap and that each new circle remains distinct, maintaining a minimum set distance from the preceding ones. As circles are drawn, the cumulative volume ratio is computed at every stage, and the randomization process concludes once the targeted total volume ratio is attained. However, a challenge arises when modeling each composite according to actual specimen dimensions; the necessity for a vast quantity of random circles not only is time-consuming but also introduces complexity due to the excessive number of elements, complicating the convergence of the analysis. Take, for example, a GB15 test specimen measuring 23×9 mm, which necessitates a matrix incorporating $292{,}845$ randomly scattered microspherical particles. Given this, the model's area is scaled down to a quarter of the real specimen's size to mitigate the computational load. To ensure the accuracy and consistency of results, multiple simulations featuring varied random inclusions are executed, establishing the reliability of the outcomes obtained under these modified parameters.

The uniaxial compression simulations for GB15 are conducted on a 2D macrostructure, measuring 10×5 mm, defined by a matrix populated with $70{,}736$ randomly distributed microspherical particles of 30 μm diameter [2]. These particles constitute 15% of the test specimen's volume. Upon completion of the model, it incorporates a total of $817{,}108$ linear 3-node triangular elements for both the matrix and fillers, each with an approximate size of 0.05 mm. Static Uniform Boundary Conditions (SUBC) are then applied, imposing a maximum displacement of 0.9 mm in the uniaxial direction [2]. Figure 7 illustrates the detailed micromechanical finite element model of the composite.

GB, being significantly stiffer than the matrix, is characterized by a linear elastic mechanical behavior, defined by a modulus of elasticity of 3546 MPa and a Poisson's ratio of 0.2. As

illustrated in Part 3 Figure 6, the introduction of GB enhances the strength of the composite beyond that of pure rubber, underscoring the beneficial impact of adding such reinforcements. The behavior of the recycled rubber matrix is encapsulated through standard J2 plasticity with non-linear hardening [65].

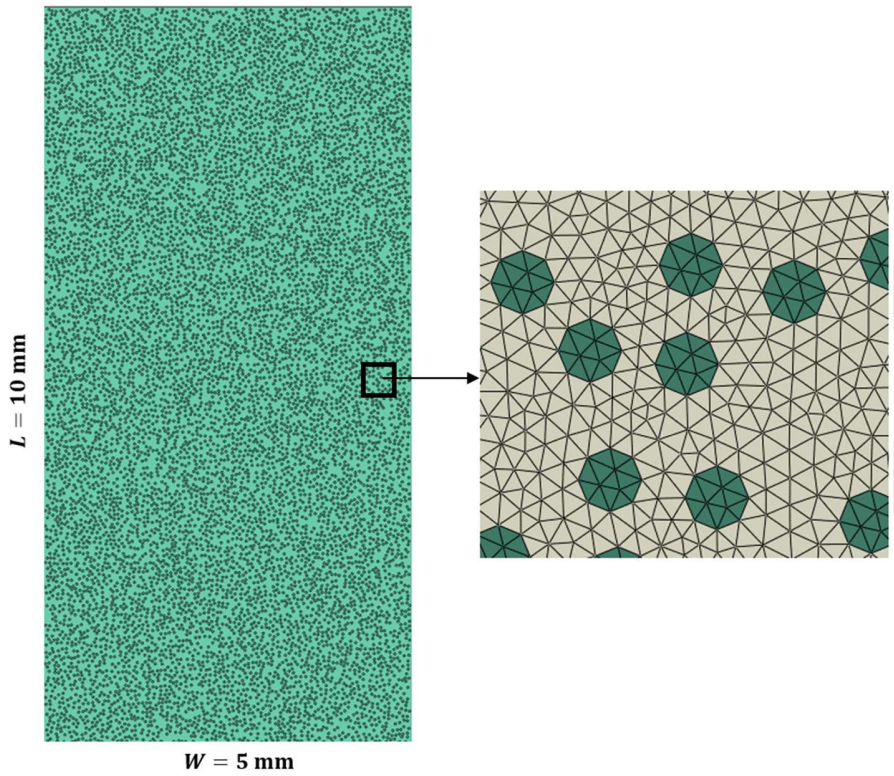

Figure 7. Macromechanical FE model of RR based composite filled with 15% GBs

To anticipate the degradation of the rubber matrix, the ductile damage initiation criterion is employed. This criterion is instrumental in pinpointing the onset of damage and is predicated on the assumption that equivalent plastic strain at damage onset, denoted as $\bar{\epsilon}_D^{pl}$, is contingent upon stress triaxiality and strain rate, expressed mathematically as $\bar{\epsilon}_D^{pl}(\eta, \dot{\epsilon}^{pl})$. Here, $\eta = -p/q$ represents stress triaxiality, where 'p' is the pressure stress and 'q' is the Mises equivalent stress; $\dot{\epsilon}^{pl}$ designates equivalent plastic strain rate. Onset of damage is confirmed when specific conditions, rooted in these parameters, are fulfilled.

$$\omega_D = \int \frac{\bar{\epsilon}^{pl}}{\bar{\epsilon}_D^{pl}(\eta, \dot{\epsilon}^{pl})} = 1 \qquad 4$$

where ω_D represents a state variable increasing with plastic deformation. In each step, the incremental change in ω_D:

$$\Delta\omega_D = \int \frac{\Delta d\bar{\epsilon}^{pl}}{\bar{\epsilon}_D^{pl}(\eta, \dot{\epsilon}^{pl})} \geq 0 \qquad 5$$

In simulating ductile damage initiation in Abaqus, the process begins with identifying ductile damage onset through an analysis of stress-strain responses obtained from compression tests. Following this initial step, the material properties are modified within the Abaqus framework to integrate the calibrated ductile damage initiation parameter. Once the material properties are updated, simulations are executed in Abaqus to observe the model's response under various loading conditions. The simulation outcomes are closely examined, offering insights into the model's behavior as it undergoes deformation. To validate the accuracy of the ductile damage initiation parameter, a comparison is conducted between the simulation results and experimental data. This validation process is iterative, allowing for the refinement of the parameter until a satisfactory alignment between numerical and experimental responses is achieved.

Within this approach, the computation of the ductile damage initiation parameter stands at 0.03979. The simulations incorporate a displacement-type damage evolution mechanism characterized by exponential softening. Additionally, the displacement at failure is set to 0.0214, governed by an exponential law parameter of 5. This ensures a robust simulation of ductile damage initiation, aligning the model behavior with the experimental results.

The failure of the specimens is associated with shear localization, where the material undergoes intense deformation in localized zones These shear bands contribute to the overall failure mechanism, providing additional insights into the material's behavior under uniaxial loading conditions. Notably, in the simulations, ductile damage contributes to the formation of shear bands as indicated by strain contours to be presented in Figures 10-14.

Figure 8 compares the numerical macroscopic axial response of the composite to the corresponding experimental data. The modeling of the microstructure using the Representative Volume Element (RVE) is applied to address homogenization problems. The RVE must be large enough to capture most of the micro-heterogeneities while maintaining a manageable size, allowing it to be treated as a continuum mechanics volume element. In theory, the RVE's behavior should be independent of the type of BCs used [66,67]. However, PBCs are selected for this study as they offer a reasonable approximation of the effective moduli. PBCs preserve the shape and alignment of opposing edges during deformation, with stress vectors on opposite sides directed oppositely to ensure continuity of stress across the boundaries [33].

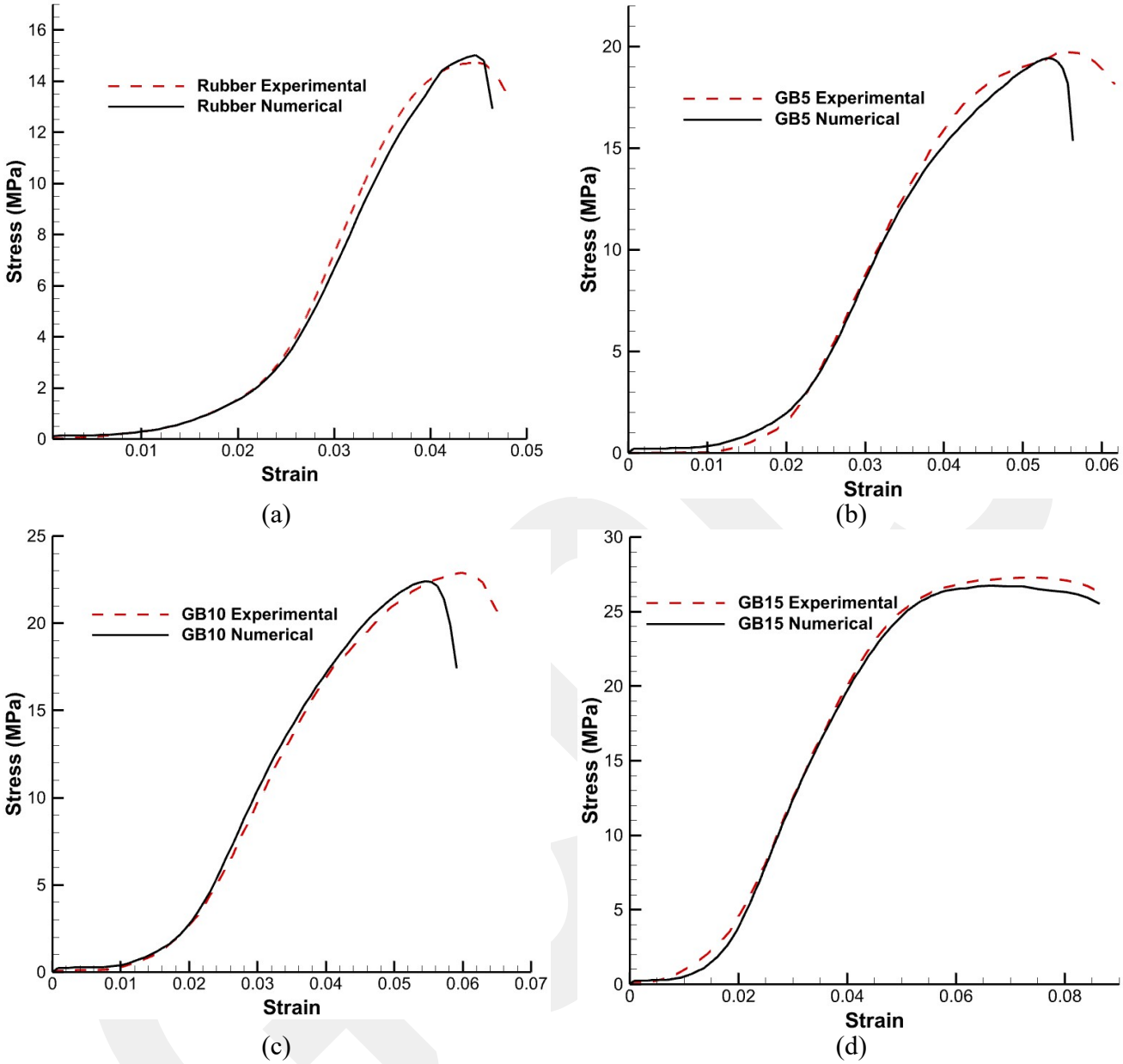

Figure 8. Experimental and numerical results of (a) pure rubber and composites (b) GB5, (c) GB10, (d) GB15

A 2D RVE with randomly distributed GBs is used in the homogenization process. To impose PBCs to the RVE, the model must have both a periodic geometry and mesh. To achieve this, a Python script is utilized to randomize the distribution of inclusions within a square domain while ensuring the geometry remains periodic. A volume element, denoted as V, is taken into consideration, and PBCs are imposed on the boundary δV to assess the overall properties.
The compression test results are replicated using distance-controlled PBCs for GB inclusions at volume fractions $V_f = 0.05, 0.10, 0.15$.
The constitutive behavior of heterogeneous structures can be captured for large volumes with

only a few realizations [66]. Accordingly, a primary objective is to analyze a 2D model with actual specimen dimensions using a limited number of realizations. Macroscopic stresses and strains, representing the mechanical properties at a macroscopic material point, are regarded as averaged values computed over a defined volume that includes the microscopic fields [68]. Macroscopic homogeneity is established by assuming that the average strain and stress are spatially independent. The stress and strain averages over a specific volume are denoted using square brackets. More specifically, if the position vector is **x**, the volume-averaged stresses and strains, denoted by square brackets, are calculated as the mean of point stresses or strains within the volume V, as expressed by [66,69].

$$\mathbf{E} = \langle \boldsymbol{\epsilon} \rangle = \frac{1}{V} \int_V \boldsymbol{\epsilon} \, \mathrm{dV} \tag{6}$$

here **E** is a symmetrical second-rank tensor, and the macroscopic stress tensor:

$$\boldsymbol{\Sigma} = \langle \boldsymbol{\sigma} \rangle = \frac{1}{V} \int_V \boldsymbol{\sigma} \, \mathrm{dV} \tag{7}$$

Using Equations 6 and 7, a Python script is developed to perform volume integration, allowing for the evaluation of average stress and strain values for each integration point at each step [2]. This approach provides a numerical response for the heterogeneous composite with V.
The principle of overall average homogenization method is the use of fourth-order concentration tensors, which establish a relationship between volume-averaged strains and stresses or the applied BCs. The strain averaged over the inclusion phase is connected to the overall macroscopic strain and the averaged strain in the matrix through the fourth-order strain concentration tensor field $\mathbb{A}$ for PBC problems [66]:

$$\boldsymbol{\epsilon}(\mathbf{x}) = \mathbb{A}(\mathbf{x}) : \mathbf{E} \tag{8}$$

a four-rank concentration tensor field $\mathbb{B}$ for SUBC problem

$$\boldsymbol{\sigma}(\mathbf{x}) = \mathbb{B}(\mathbf{x}) : \boldsymbol{\Sigma} \tag{9}$$

The concentration tensor field is equal to the fourth-rank identity tensor [66]

$$\langle \mathbb{A} \rangle = \langle \mathbb{B} \rangle = \mathbb{I} \tag{10}$$

Following numerous realizations of variously sized RVEs with PBCs, the macroscopic strain and stress tensors are computed for each volume element. Then, within the macroscopic structure utilizing SUBC, the average stress and strain values are calculated.

To determine the optimum RVE size, RVE size estimation process is utilized. This involves conducting multiple randomizations for the composites, employing a range of RVE sizes to systematically evaluate their responses. This process is visually illustrated in Figure 9.
Additionally, Table 4 presents the number of randomized inclusions associated with the length of the volume element, used in defining the RVE size, along with the number of realizations considered for each RVE length.

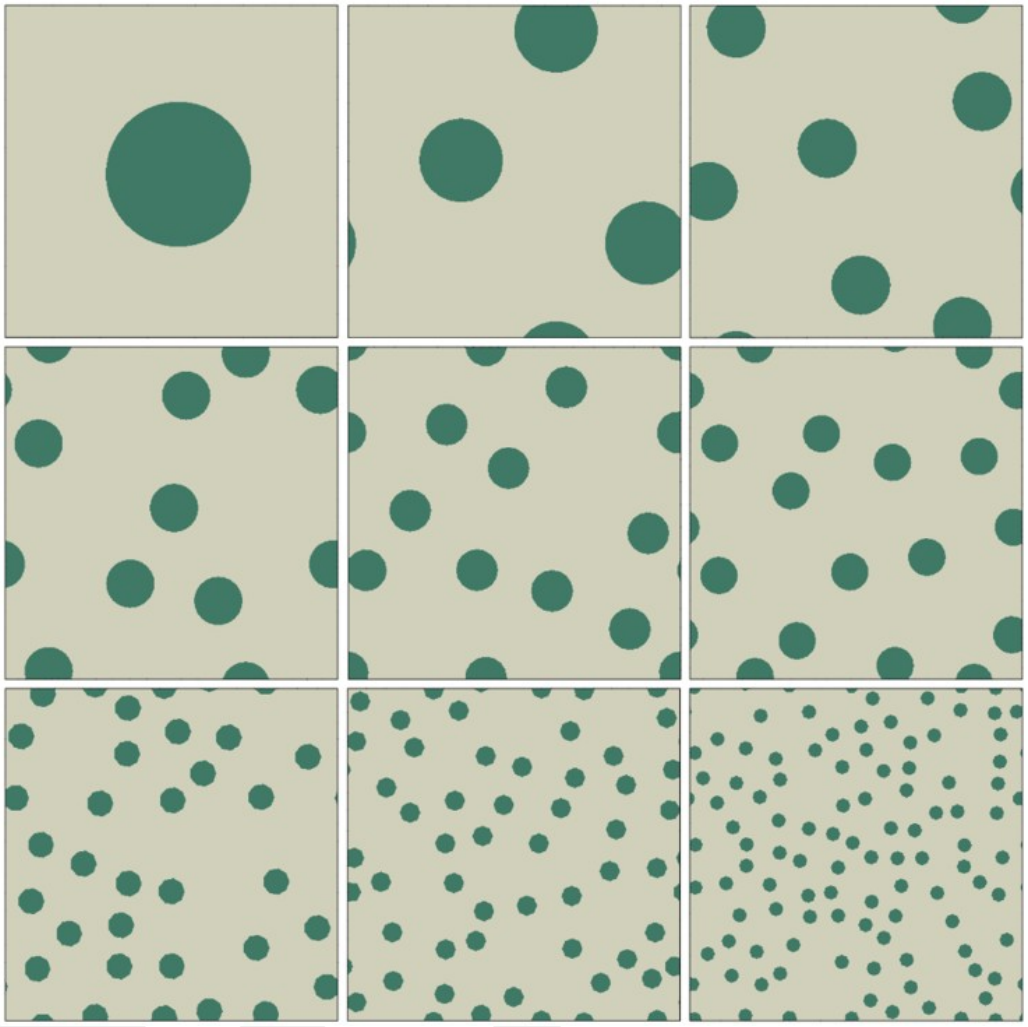

Figure 9. Randomization of RVE with different sizes for GB composites (V_f = 0.15) [2]

Table 4. Length of RVEs with the number of randomized GBs

Volume fraction, V_f (%)	**RVE size, L (μm)**	**# of inclusions, N**	**# of realizations, n**
5	205	3	15
5	238	4	12
5	266	5	10
5	291	6	7
10	206	6	11
10	238	8	9
10	266	10	7
10	291	12	5
15	69	1	1
15	119	3	8
15	168	6	6
15	206	9	5
15	238	12	23
15	266	15	19
15	376	30	17
15	485	50	14
15	574	70	12
15	687	100	8

The results of RVEs of varying sizes are illustrated in Figures 10, 11 and 2, with a comparative view against the experimental test result for $V_f = 0.15$. Figure 10 presents RVEs with L = 69 µm and L = 119 µm and Figure 11 with L = 206 µm and L = 238 µm, while Figure 12 illustrates RVEs with L = 376 µm and L = 687 µm. Upon closer examination, it becomes evident that the RVE with L = 69 µm deviates significantly from the experimental stress-strain curve, signifying an inadequate representation of the material's behavior at this size. Although L = 119 µm demonstrates closer alignment with the experimental observations, it falls short of accurately reflecting the behavior of the material. L = 206 µm exhibits improved agreement with the experimental curve; however, the RVE with L = 238 µm provides the most optimal curve fitting to the macroscale response. The choice of L = 238 µm is guided by the fundamental principle that an RVE size must be small enough to capture microstructural details and, simultaneously, large enough to offer a representative characterization of the material. In this context, the 238 µm RVE strikes a balance, comprising essential microstructural features and leading to a more precise representation of the material's macroscopic behavior. The comparative analysis serves as a critical evaluation of different RVE sizes, emphasizing the need for precision in choosing an RVE size that harmonizes microstructural accuracy with macroscopic representativeness. Additionally, the inclusion of RVE sizes 376 µm and 687 µm in Figure 12 is considered, but the 238 µm RVE is deemed sufficient, reconfirming the consistence required for an optimal representation of microstructure and macroscopic behavior. Figure 13 presents the cumulative results across various sizes of RVEs, allowing for a direct comparison. It becomes evident from this figure that selecting the optimal size as 238 µm is the appropriate choice. The estimation of RVE length is done for a volume fraction of 0.15. The expected RVE size encompasses the sizes for $V_f = 0.05$ and $V_f = 0.10$. Essentially, the

238 µm RVE size is suitable for these volume fractions as it captures sufficient information on microstructure and remains significantly smaller than the macroscopic structural dimensions.

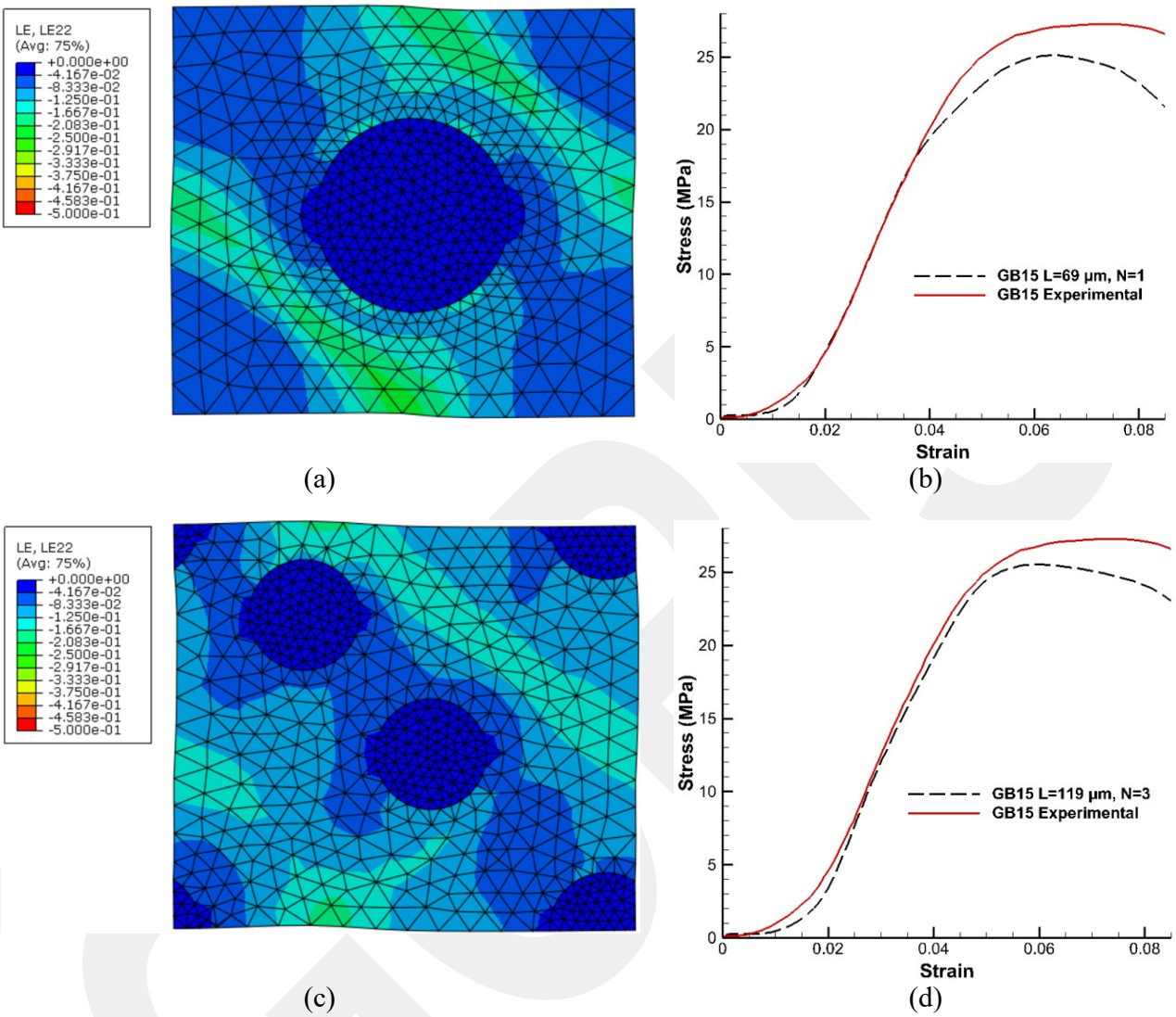

Figure 10. Strain contours of RVE with (a) L = 69 µm and (c) L = 119 µm for $V_f = 0.15$, Numerical and experimental results for (b) L = 69 µm and (d) L = 119 µm

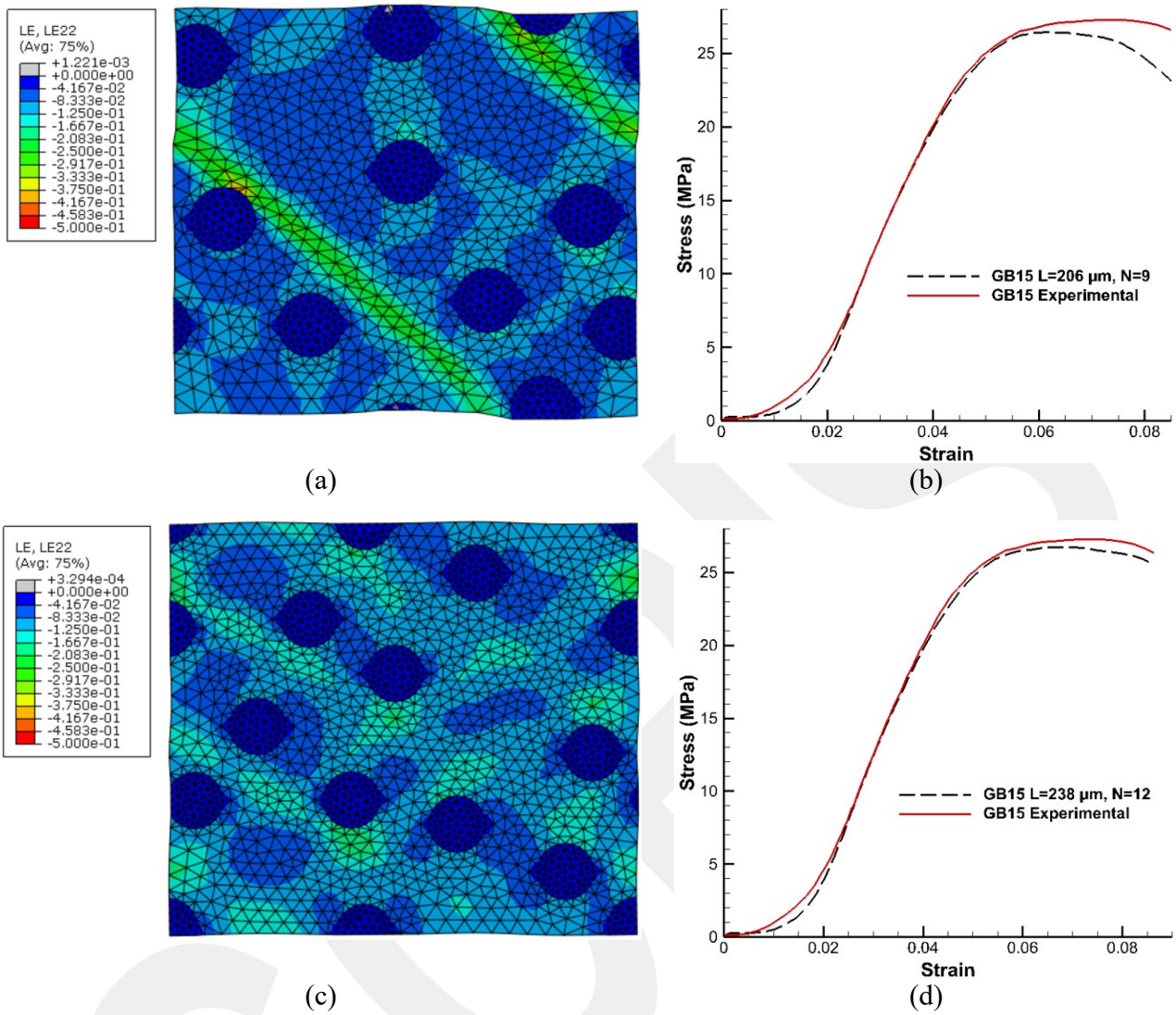

Figure 11. Strain contours of RVE with (a) L = 206 µm and (c) L = 238 µm for $V_f = 0.15$, Numerical and experimental results for (b) L = 206 µm and (d) L = 238 µm

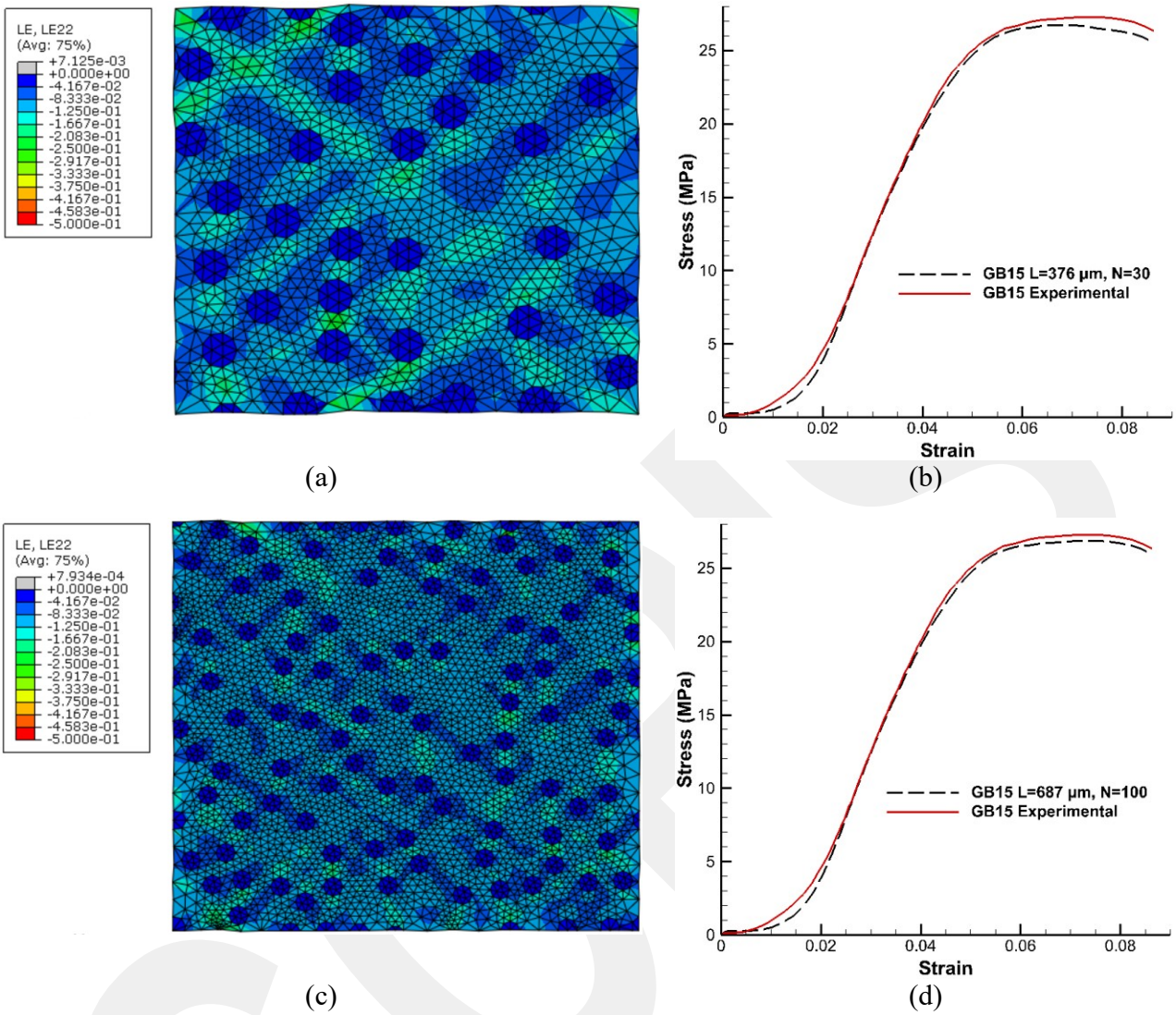

Figure 12. Strain contours of RVE with (a) L = 376 µm and (c) L = 687 µm for $V_f = 0.15$, Numerical and experimental results for (b) L = 376 µm and (d) L = 687 µm

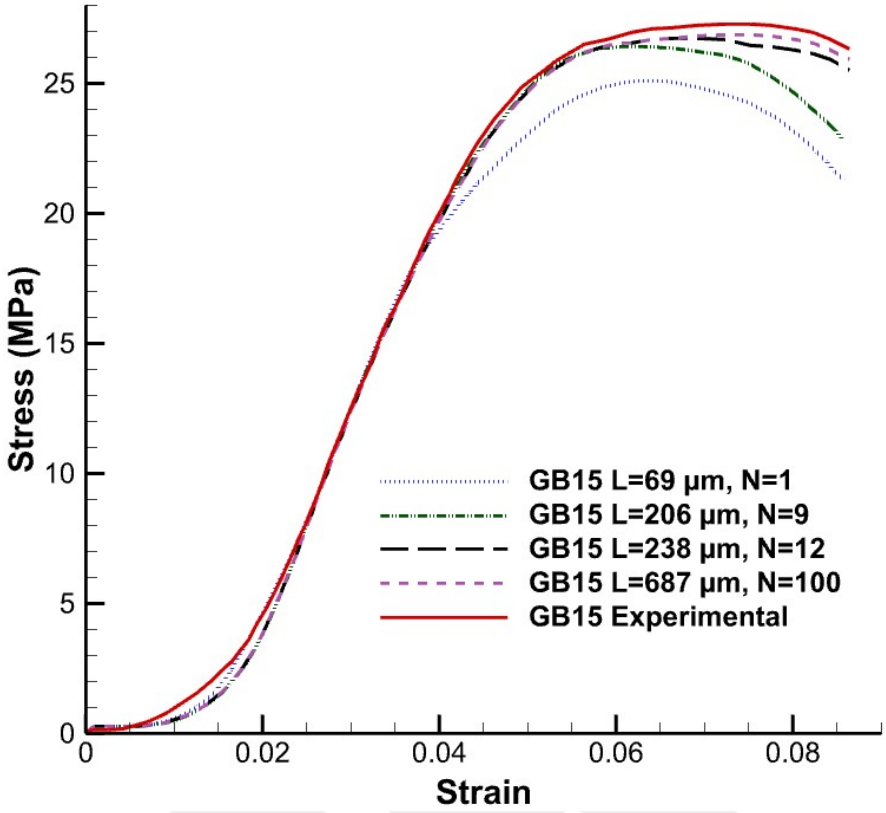

Figure 13. Comparison of responses across different RVE sizes as provided in Table 4 ($V_f = 0.15$)

The numerical results are conducted with varying arrangements to assess the impact of GB distributions. This approach allows to analyze how different configurations of inclusions affect the overall outcome. For the specified RVE length, multiple realizations are conducted with various distributions of the inclusions. As an example, logarithmic strain contours along direction 2 and a comparison of the responses are illustrated in Figure 13 for the optimal RVE length of 238 µm. It can be concluded that the distribution of inclusions has a negligible impact on the numerical results.

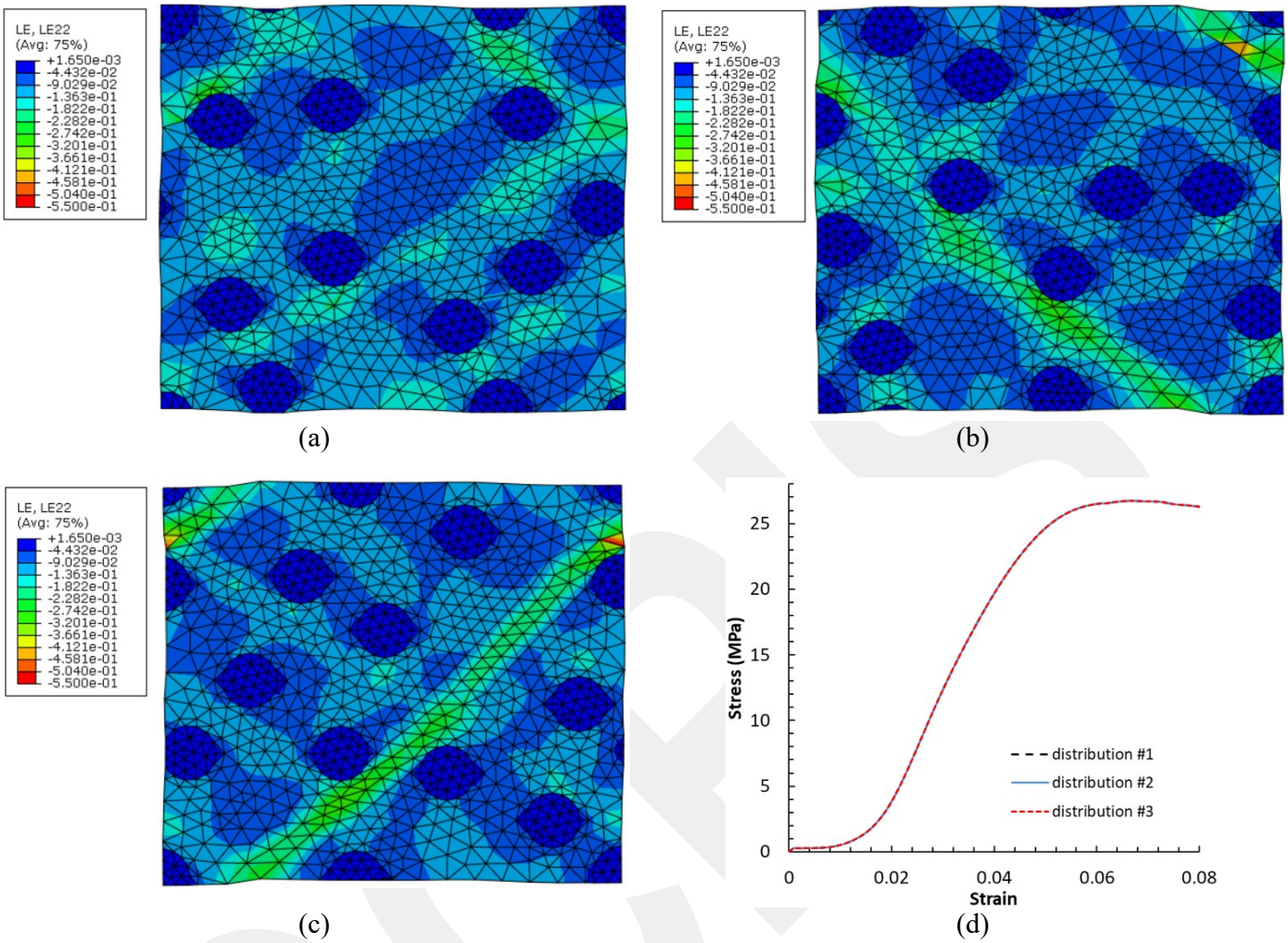

Figure 14. Strain contours for the RVE with L = 238 µm for different random distributions of GBs (a) Distribution #1 (b) Distribution #2 (c) Distribution #3 (d) Comparison of the responses (V_f = 0.15)

Across all analyses, the average diameter of GBs is estimated to be 30 µm. To demonstrate the impact of varying diameters of GBs, numerical analyses are conducted for the anticipated RVE size ($L = 238\ \mu m$), featuring GBs of $30, 40$, and 50 µm diameters, as depicted in Figure 15. Inclusions with sizes spanning from 20 to 50 µm and from 10 to 60 µm are also modeled (Figure 16). Interestingly, variations in inclusion sizes appear to have minimal influence on the numerical outcomes. While the study by Li et al. [70] found that the size of the reinforcements has a noticeable impact on the mechanical properties of composites, the numerical analysis conducted in this study indicated that variations in the glass bubble sizes (30, 40, and 50 µm) had minimal effect on the stress-strain response. This contrast suggests that for recycled rubber composites, the homogeneity of the matrix and reinforcement distribution may play a more critical role than the size of the inclusions.

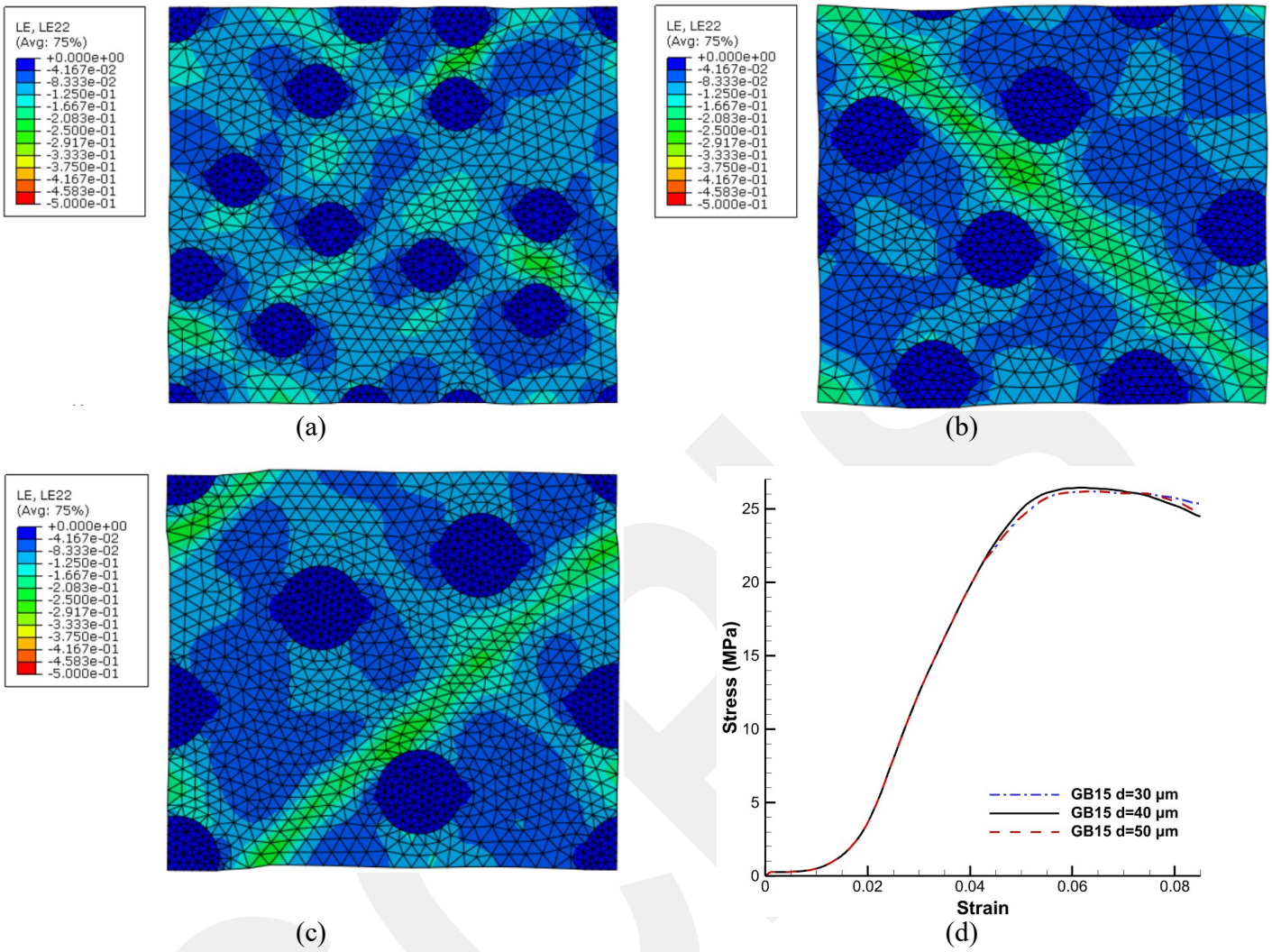

Figure 15. Strain contours for RVE with L = 238 μm in the compression direction with GB diameter of (a) d = 30 μm, (b) d = 40 μm, (c) d = 50 μm and (d) comparison of the responses for $V_f = 0.15$

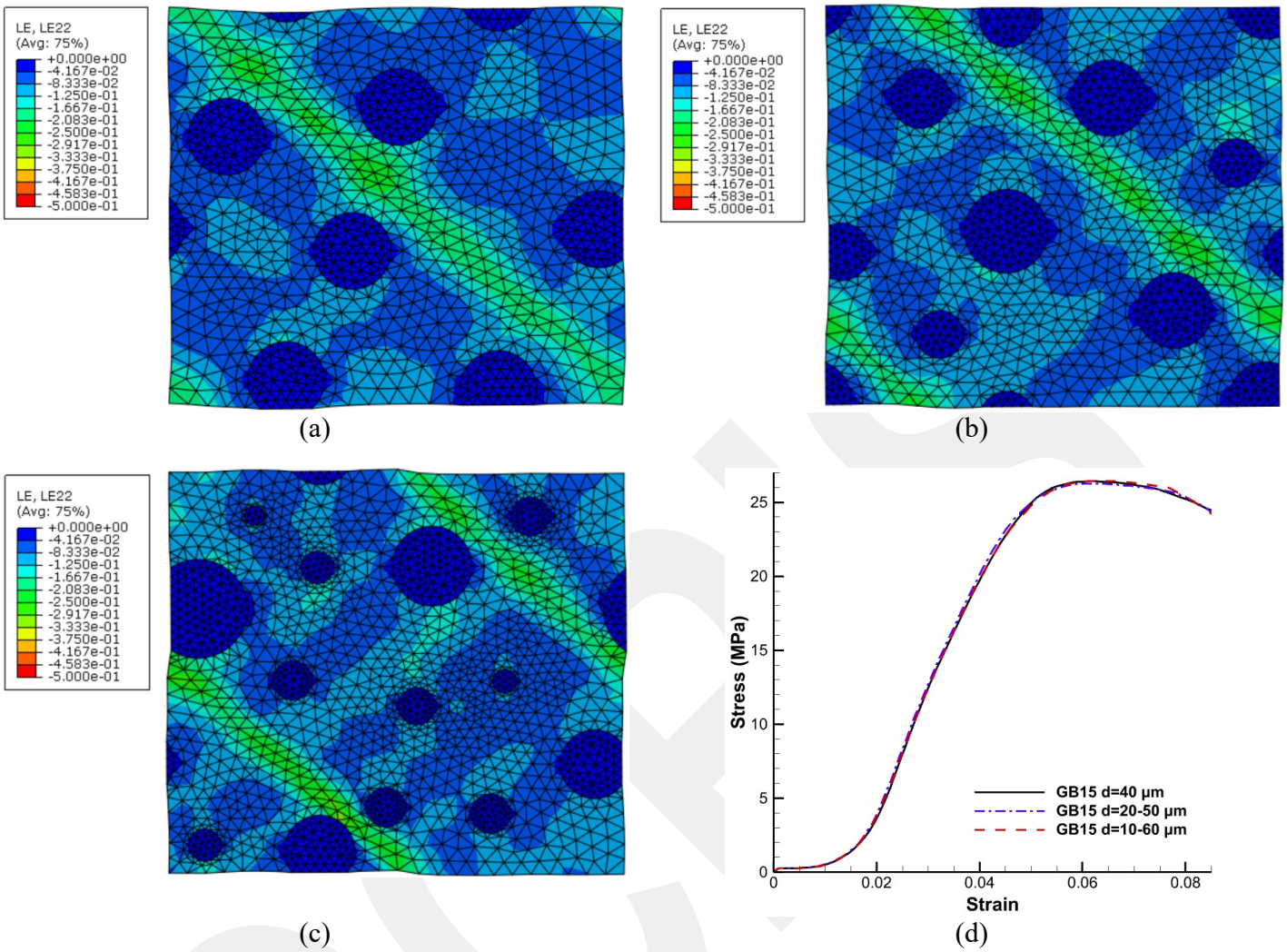

Figure 16. Strain contours for RVE in the compression direction with GB diameter of (a) d = 40 µm, (b) d = 20 − 50 µm, (c) d = 10 − 60 µm and (d) comparison of the responses for $V_f = 0.15$

Figure 17 shows the deformed geometry of RVEs with various volume fractions under distance-controlled PBCs. The alignment between experimental test results and numerical simulations, as depicted in Figure 17, is further detailed in Table 5. When the composite undergoes compression, it becomes evident that the failure mechanism predominantly involves shear. This observation is further corroborated by our simulation results, which demonstrate that the reinforcements may influence the localization path but do not fundamentally alter the direction of the shear-dominated failure mode (see Fig. 18). It is fair to conclude that the results demonstrate consistency with macroscopic responses.

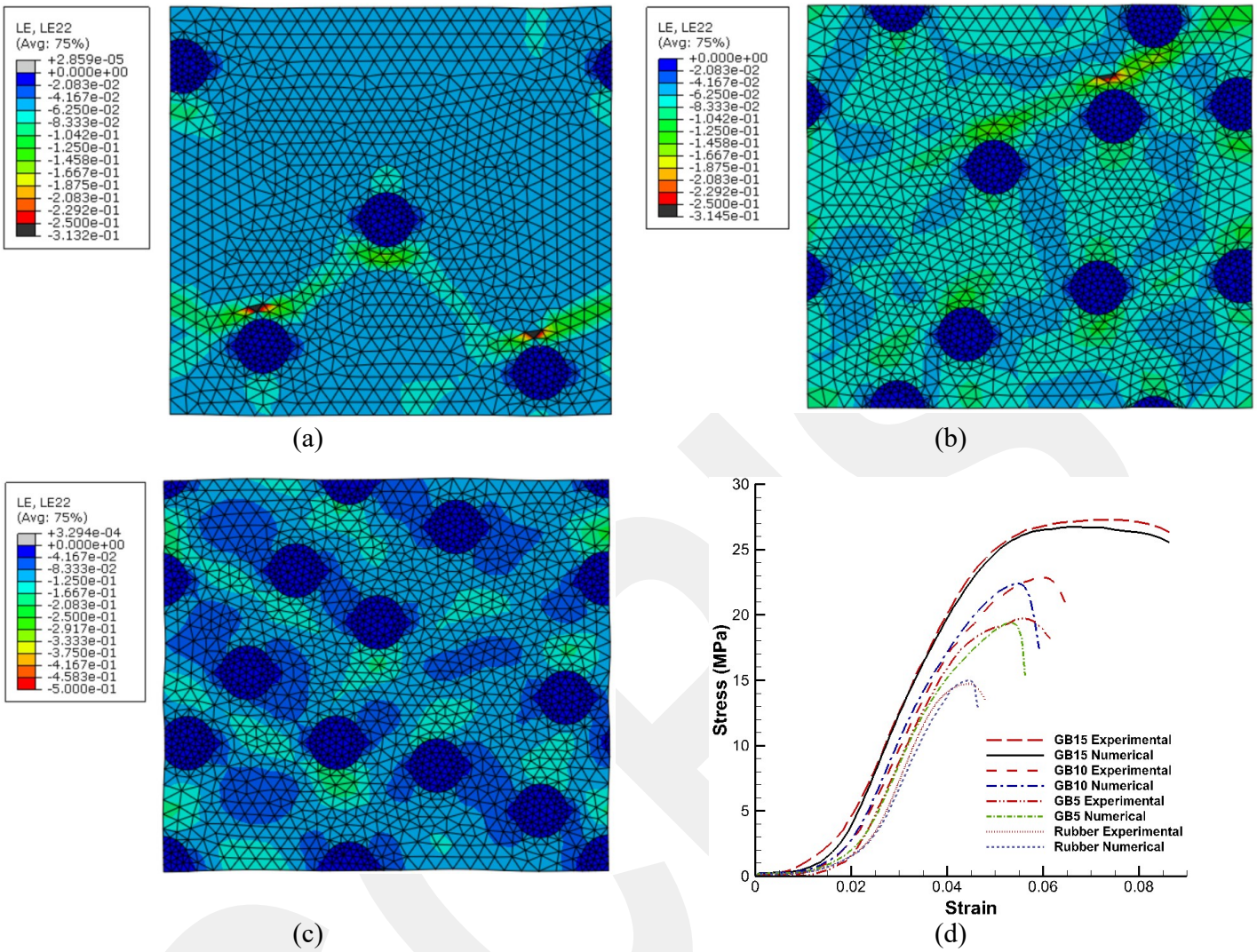

Figure 17. Strain contours of the composites for (a) $V_f = 0.05$, (b) $V_f = 0.10$, (c) $V_f = 0.15$ and (d) comparison of the responses with experimental results (L = 238 μm)

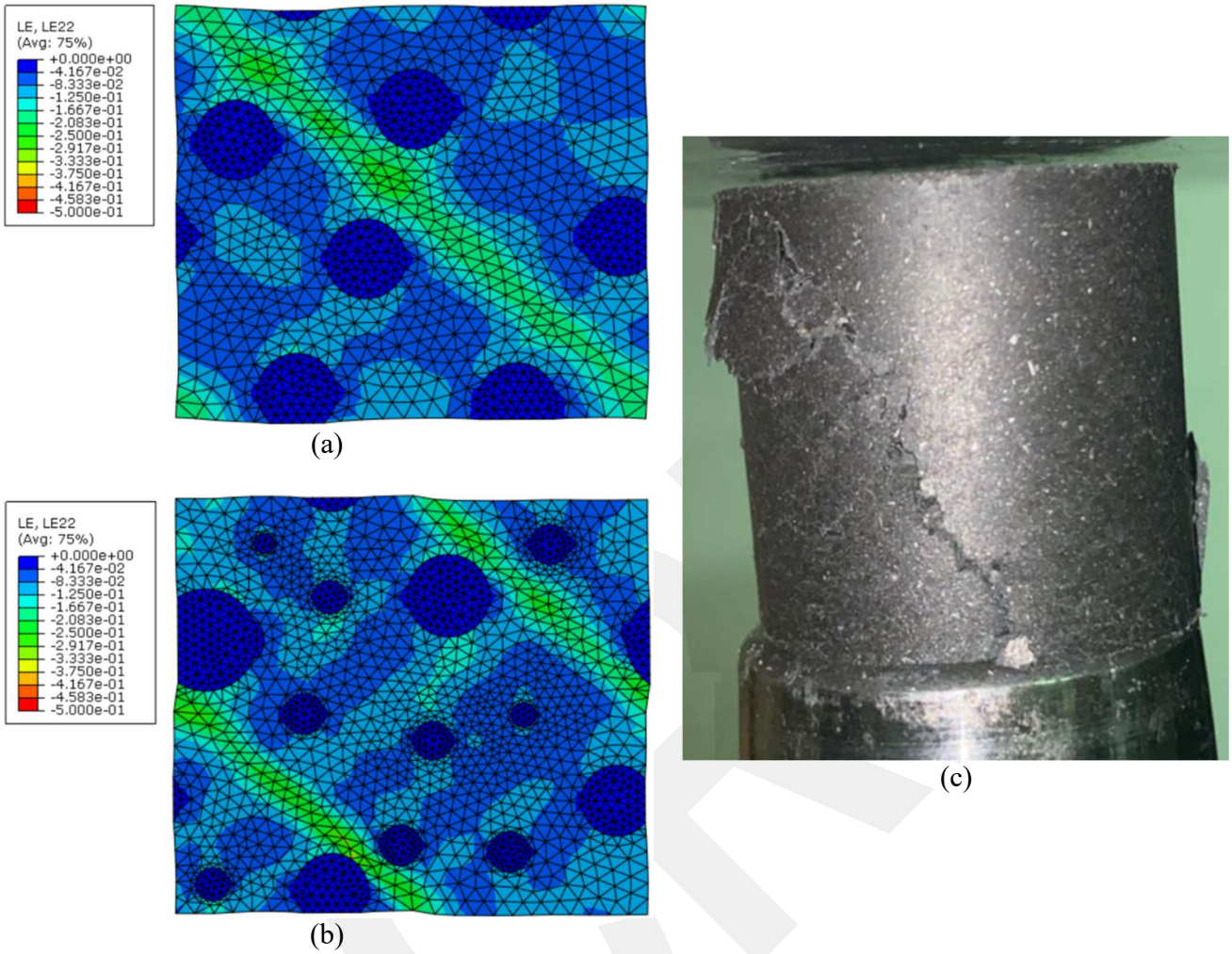

Figure 18. The comparison between the RVE with GB diameter of (a) d = 40 μm, (b) d = 10 − 60 μm and (c) the failure characteristics of the specimen

Table 5. Comparison of the experimental test results and numerical simulations for uniaxial compression tests

Composite Name	Ultimate Stress, σ_u (MPa) (experimental)	Ultimate Stress, σ_u (MPa) (numerical)	Strain at Break, ϵ_f (%) (experimental)	Strain at Break, ϵ_f (%) (numerical)
Matrix	14.74	15.01	4.80	4.64
GB5	19.72	19.28	6.16	5.45
GB10	22.88	22.39	6.53	5.91
GB15	27.27	26.60	8.64	8.73

5. Conclusion

This study sets out to design a devulcanized RR based composite, fortified with micro glass bubble (GB) reinforcements, and subsequently develop a numerical model that is validated by experimental results for such rubber-based reinforced composites. The experimental outcomes distinctly showcase an enhancement in the mechanical characteristics of the rubber-based matrix due to the inclusion of glass bubble reinforcements. Specifically, the addition of GBs resulted in improved strength and stiffness, which are critical for applications requiring lightweight yet durable materials. Moreover, it is noticed that the volume ratio of the GBs significantly influences these mechanical properties, whereas fluctuations in the GB size seemingly have negligible effect. In other words, variations in GB size (30, 40, and 50 μm) are demonstrated to have an insignificant impact on the mechanical properties, suggesting that overall composite response is more dependent on GB volume than size. This finding suggests that the reinforcement process can focus on optimizing volume fraction without the need to account for detailed size variations, simplifying manufacturing processes.
Numerical simulations for RR composite, reinforced with GBs, were performed using ABAQUS/Standard, placing a particular emphasis on stress and strain measurements in the axial direction. These simulations provided crucial insights into the stress distribution within the composite, showing that the inclusion of GBs leads to uniform stress distribution across the matrix. The robustness of the numerical approach is confirmed through its successful comparison with the experimental findings, validating the model's capability to predict real-world performance. The combined experimental and numerical analysis presents a comprehensive understanding of the behavior of reinforced recycled rubber composites. The key findings highlighted in the paper are summarized below:

- Manufacturing of devulcanized RR based composites incorporating micro glass bubble (GB) reinforcements with a density of 0.65 g/cm³ and a modulus of elasticity of 3.5 GPa, facilitating substantial weight reduction with a high strength-to-density ratio.
- Conducting uniaxial compression tests with different volume fractions of inclusions (5%, 10%, and 15%) in matrix significantly influences mechanical properties of composites.
- RVE with unit length of 238 μm is expected to exhibit the most effective adjustment to the macroscale response.
- The variation in the diameter of GB (30, 40, and 50 μm) does not significantly impact the numerical results, suggesting robustness in the material response.
- Devulcanized recycled rubber can be substantially strengthened through the incorporation of appropriate inclusions, a fact that can also be validated through numerical analysis.

Overall, the study demonstrates the effectiveness of GB-reinforced devulcanized recycled rubber composites through comprehensive experimental and numerical investigations. The findings provide valuable insights for future material designs, particularly in industries seeking lightweight, high-strength, and cost-effective solutions. This research contributes to the growing body of knowledge on sustainable composites, offering a pathway to enhancing recycled materials without compromising performance.

References

1. Low, D.Y.S.; Supramaniam, J.; Soottitantawat, A.; Charinpanitkul, T.; Tanthapanichakoon, W.; Tan, K.W.; Tang, S.Y. Recent Developments in Nanocellulose-Reinforced Rubber Matrix Composites: A Review. Polymers 2021, 13, 550.
2. Kabakci, G.C.; Toughening Mechanism Analysis of Recycled Rubber Based Composites Reinforced with Glass Bubbles and Alumina Fibers. PhD thesis, CY Cergy Paris Université, 2023.
3. Zang, R., Xu, B. W., & Zhang, K. Y. (2022). Properties of Self-compacting Concrete Incorporating Recycled Tyre Rubber Particles. Journal of Cleaner Production, 262, 716–733.
4. Chang, B. P., Gupta, A., Muthuraj, R., & Mekonnen, T. H., Bioresourced fillers for rubber composite sustainability: current development and future opportunities. Green Chemistry, 2021, 23(15), 5337-5378.
5. Low, D.Y.S.; Supramaniam, J.; Soottitantawat, A.; Charinpanitkul, T.; Tanthapanichakoon, W.; Tan, K.W.; Tang, S.Y. Recent Developments in Nanocellulose-Reinforced Rubber Matrix Composites: A Review. Polymers 2021, 13, 550.
6. Kabakci, G.C.; Aslan, O.; Bayraktar, E. A Review on Analysis of Reinforced Recycled Rubber Composites. Journal of Composites Science 2022, 6. https://doi.org/10.3390/jcs6080225.
7. Irez, A.B.; Bayraktar, E.; Miskioglu, I. Recycled and devulcanized rubber modified epoxy-based composites reinforced with nano-magnetic iron oxide, Fe3O4. Composites Part B: Engineering 2018, 148, 1–13. https://doi.org/https://doi.org/10.1016/j.compositesb.2018.04.047.
8. Heidari, M.; Mozaffari, M.; Beheshti, H. Advances in Devulcanization Processes for Rubber Recycling. Polymer Recycling Journal 2022, 15, 101-120.
9. Zaghloul, M.M.Y.; Mohamed, Y.S.; El-Gamal, H. Fatigue and tensile behaviors of fiber-reinforced thermosetting composites embedded with nanoparticles. Journal of Composite Materials 2019, 53, 709–718, https://doi.org/10.1177/0021998318790093.
10. Wang, Z.; Zhang, P.; Li, Y. Mechanical Properties of Devulcanized Rubber under Strain. Materials Science Journal 2023, 40, 199-215.
11. Irez, A.; Bayraktar, E.; Miskioglu, I. Design and Mechanical-Physical Properties of Epoxy-Rubber Based Composites Reinforced with Nanoparticles. Procedia Engineering 2017, 184, 486–496. Advances in Material & Processing Technologies Conference, https://doi.org/https://doi.org/10.1016/j.proeng.2017.04.119.
12. Cao, X.; Jiang, Y.; Liu, Z. Microscale Reinforcements in Rubber Composites. *Composites Science* 2021, *58*, 276-290.
13. Irez, A.B.; Zambelis, G.; Bayraktar, E. A New Design of Recycled Ethylene Propylene Diene Monomer Rubber Modified 315 Epoxy Based Composites Reinforced with Alumina Fiber: Fracture Behavior and Damage Analyses. Materials 2019, 12. 316 https://doi.org/10.3390/ma12172729.
14. Hasan, R.; Ali, A.; Ahmed, F. Utilizing Nano-silica in Recycled Rubber Composites. Nanotechnology in Polymers 2023, 18, 45-68.
15. Liang, J.; Zhao, H.; Chen, Z. Reinforcing Recycled Rubber with Carbon Nanotubes. Composite Materials 2022, 36, 213-228.
16. Ma, L.; Sun, Y.; He, J. Enhancing the Mechanical Properties of Recycled Rubber. Composite Structures 2021, 54, 102-119.

17. Ferreira, L. M. P., Bayraktar, E., Miskioglu, I., & Robert, M. H. Design and physical properties of multifunctional structural composites reinforced with nanoparticles for aeronautical applications. Advances in Materials and Processing Technologies, 2016, 3(1), 33–44. https://doi.org/10.1080/2374068X.2016.1247243

18. Rana, A. S., Vamshi, M. K., Naresh, K., Velmurugan, R., & Sarathi, R. Mechanical, thermal, electrical and crystallographic behaviour of EPDM rubber/clay nanocomposites for out-door insulation applications. Advances in Materials and Processing Technologies, 2019, 6(1), 54–74. https://doi.org/10.1080/2374068X.2019.1703339

19. Dhingra, A.K.; Peacock, N.; Ubbelohde, A.R.J.P.; Manfre, C.; Watt, W.; Harris, B.; Ham, A.C. Alumina fibre FP. Philosophical Transactions of the Royal Society of London. Series A, Mathematical and Physical Sciences 1980, 294, 411–417, [https://royalsocietypublishing.org/doi/pdf/10.1098/rsta.1980.0049]. https://doi.org/10.1098/rsta.1980.0049.

20. Kabakci, G.C.; Aslan, O.; Bayraktar, E. Toughening Mechanism Analysis of Recycled Rubber-Based Composites Reinforced with Glass Bubbles, Glass Fibers and Alumina Fibers. Polymers 2021, 13. https://doi.org/10.3390/polym13234215.

21. Sun S, et al. (2022). Hollow Glass Microspheres as High-Strength Fillers for Composite Reinforcement. Journal of Polymer Research.

22. Ma J, Zhang Y, et al. (2022). Constructing Nanocomposites with Robust Covalent Connections for High Discharge Energy and Enhanced Tensile Properties. Journal of Energy Chemistry.

23. Geim, A.; Novoselov, K. The Rise of Graphene. Nature materials 2007, 6, 183–91. https://doi.org/10.1038/nmat1849.

24. Platzer, N. Fracture mechanics of polymers, J. G. Williams, Halsted Press, New York, 1984, 302 pp. Price: $39.95. Journal of Polymer Science: Polymer Letters Edition 1985, 23, 195–195, [https://onlinelibrary.wiley.com/doi/pdf/10.1002/pol.1985.130230405]. https://doi.org/https://doi.org/10.1002/pol.1985.130230405.

25. Zhang, Z.; Lei, H. Preparation of α-alumina/polymethacrylic acid composite abrasive and its CMP performance on glass substrate. Microelectronic Engineering 2008, 85, 714–720. https://doi.org/https://doi.org/10.1016/j.mee.2008.01.001.

26. Zhang, G.; Wang, F.; Dai, J.; Huang, Z. Effect of Functionalization of Graphene Nanoplatelets on the Mechanical and Thermal Properties of Silicone Rubber Composites. Materials 2016, 9. https://doi.org/10.3390/ma9020092.

27. Gupta, N. Reinforced Polymer Matrix Syntactic Foams Effect of Nano and Micro-Scale Reinforcement, 1st ed. 2013. ed.; SpringerBriefs inMaterials, Springer International Publishing: Cham, 2013.

28. 3M Glass Bubbles K Series, S Series and iM Series. https://multimedia.3m.com/mws/media/91049O/3m-glass-bubbles-k-s-and-im-series.pdf, 2021.

29. Râpa, M.; Spurcaciu, B.N.; Coman, G.; Nicolae, C.A.; Gabor, R.A.; Ghioca, P.N.; Berbecaru, A.C.; Matei, E.; Predescu, C. Effect of Styrene-Diene Block Copolymers and Glass Bubbles on the Post-Consumer Recycled Polypropylene Properties. Materials 2020, 13. https://doi.org/10.3390/ma13030543.

30. Kabakci, G.C.; Aslan, O.; Bayraktar, E. Toughening Mechanism Analysis of Recycled Rubber-Based Composites Reinforced with Glass Bubbles, Glass Fibers and Alumina Fibers. Polymers 2021, 13. https://doi.org/10.3390/polym13234215.

31. K-Çakır, G.; Aslan, Ö.; Bayraktar, E. Toughening Mechanism of Recycled Rubber Based Composites Reinforced with Glass Fibers + Alumina Fibers for Military Applications. In Proceedings of the Mechanics of Composite, Hybrid and Multifunctional Materials, Fracture, Fatigue, Failure and Damage Evolution, Volume 3; Chalivendra, V.; Beese, A.M.; Berke, R.B., Eds.; Springer International Publishing: Cham, 2022; pp. 99–109.

32. K-Cakir, G.; Aslan, O.; Bayraktar, E. Numerical Modeling of Recycled Rubber Based Composites Reinforced with Glass Fibers at High Strain Rates. In Proceedings of the Mechanics of Composite, Hybrid and Multifunctional Materials, Fracture, Fatigue, Failure and Damage Evolution, Volume 3; Chalivendra, V.; Beese, A.M.; Berke, R.B., Eds.; Springer International Publishing: Cham, 2022; pp. 81–84.

33. Kouznetsova, V.; Brekelmans, W.; Baaijens, F. An approach to micro-macro modeling of heterogeneous materials. Computational Mechanics 2001, 27, 37–48. https://doi.org/10.1007/s004660000212.

34. Halpin, J.C. Effects of Environmental Factors on Composite Materials. 1969.

35. Mori, T.; Tanaka, K. Average stress in matrix and average elastic energy of materials with misfitting inclusions. Acta Metallurgica1973, 21, 571–574. https://doi.org/https://doi.org/10.1016/0001-6160(73)90064-3.

36. Affdl, J.C.H.; Kardos, J.L. The Halpin-Tsai equations: A review. Polymer Engineering & Science 1976, 16, 344–352, [https://4spepublications.onlinelibrary.wiley.com/doi/pdf/10.1002/pen.760160512]. https://doi.org/https://doi.org/10.1002/pen.760160512.

37. Eshelby, J.D. The Determination of the Elastic Field of an Ellipsoidal Inclusion, and Related Problems. Proceedings of the RoyalSociety of London Series A 1957, 241, 376–396. https://doi.org/10.1098/rspa.1957.0133.

38. Hashin, Z. The Elastic Moduli of Heterogeneous Materials. Journal of Applied Mechanics 1962, 29, 143–150, [https://asmedigitalcollectio3n58.asmpdf/29/1/143/5444378/143_1.pdf]. https://doi.org/10.1115/1.3636446.

39. Hashin, Z.; Shtrikman, S. A variational approach to the theory of the elastic behaviour of multiphase materials. Journal of the Mechanics and Physics of Solids 1963, 11, 127–140. https://doi.org/https://doi.org/10.1016/0022-5096(63)90060-7.

40. Hill, R. A self-consistent mechanics of composite materials. Journal of the Mechanics and Physics of Solids 1965, 13, 213–222.https://doi.org/https://doi.org/10.1016/0022-5096(65)90010-4.

41. Sánchez-Palencia, E. Non-homogeneous media and vibration theory. Lecture Note in Physics, Springer-Verlag 1980, 320, 57–65.

42. Bensoussan, A.; Lions, J.L.; Papanicolaou, G. Asymptotic analysis for periodic structures; Vol. 374, American Mathematical Soc., 2011.

43. Beran, M.J. Statistical Continuum Theories. Journal of Rheology 1965, 9, 339–355.

44. Torquato, S. Random Heterogeneous Media: Microstructure and Improved Bounds on Effective Properties. Applied Mechanics Re- 367 views 1991, 44, 37–76, [https://asmedigitalcollection.asme.org/appliedmechanicsreviews/article-pdf/44/2/37/5435841/37_1.pdf]. https://doi.org/10.1115/1.3119494.

45. Milton, G.W. The coherent potential approximation is a realizable effective medium scheme. Communications in Mathematical Physics 1985, 99, 463–500.

46. Besson, J.; Cailletaud, G.; Chaboche, J.; Forest, S. Mécanique non linéaire des matériaux; Hermès Science, 2001.

47. Kröner, E. Nonlinear Elastic Properties of Micro-Heterogeneous Media. Journal of Engineering Materials and Technology 1994, 116, 325–330, [https://asmedigitalcollection.asme.org/materialstechnology/article-pdf/116/3/325/5516911/325_1.pdf]. https: //doi.org/10.1115/1.2904295.
48. Gründemann, H. Sanchez-Palencia, E.; Zaoui, A. (eds.), Homogenization Techniques for Composite Media. Proceedings, Udine, Italy 1985. Berlin etc., Springer-Verlag 1987. IX, 397 pp., DM 73,—. ISBN 3-540-17616-0 (Lecture Notes in Physics 272). ZAMM - Journal of Applied Mathematics and Mechanics / Zeitschrift für Angewandte Mathematik und Mechanik 1988, 68, 212–212, [https://onlinelibrary.wiley.com/doi/pdf/10.1002/zamm.19880680608]. https://doi.org/https://doi.org/10.1002/zamm.19880680608.
49. Nemat-Nasser, S. Micromechanics : overall properties of heterogeneous materials / by S. Nemat-Nasser, M. Hori.; North-Holland series in applied mathematics and mechanics ; v. 37, North-Holland: Amsterdam, 1993.
50. Suquet, P. Plasticite et homogenesation. PhD thesis, Université Pierre et Marie Curie, 1982.
51. Suquet, P. Elements of homogenization for inelastic solid mechanics. Homogenization techniques for composite media 1987.
52. Hill, R. Elastic properties of reinforced solids: Some theoretical principles. Journal of the Mechanics and Physics of Solids 1963, 11, 357–372. https://doi.org/https://doi.org/10.1016/0022-5096(63)90036-X.
53. Terada, K.; Kikuchi, N. Nonlinear homogenization method for practical applications. American Society of Mechanical Engineers, Applied Mechanics Division, AMD 1995, 212, 1–16. Proceedings of the 1995 ASME International Mechanical Engineering Congress and Exposition ; Conference date: 12-11-1995 Through 17-11-1995.
54. Smit, R. Toughness of heterogeneous polymeric systems : a modeling approach. PhD thesis, Mechanical Engineering, 1998. https://doi.org/10.6100/IR511910.
55. Smit, R.; Brekelmans, W.; Meijer, H. Prediction of the mechanical behavior of nonlinear heterogeneous systems by multi-levelfinite element modeling. Computer Methods in Applied Mechanics and Engineering 1998, 155, 181–192. https://doi.org/https: //doi.org/10.1016/S0045-7825(97)00139-4.
56. Miehe, C.; Schröder, J.; Schotté, J.S. Computational homogenization analysis in finite plasticity Simulation of texture developmentin polycrystalline materials. Computer Methods in Applied Mechanics and Engineering 1999, 171, 387–418.
57. Feyel, F.; Chaboche, J.L. FE2 multiscale approach for modelling the elastoviscoplastic behaviour of long fibre SiC/Ti composite materials. Computer Methods in Applied Mechanics and Engineering 2000, 183, 309–330
58. Moulinec, H.; Suquet, P. A numerical method for computing the overall response of nonlinear composites with complex microstructure. Computer methods in applied mechanics and engineering 1998, 157, 69–94.
59. Miehe, C.; Schotte, J.; Schröder, J. Computational micro–macro transitions and overall moduli in the analysis of polycrystals atlarge strains. Computational Materials Science 1999, 16, 372–382.
60. Miehe, C.; Schotte, J.; Lambrecht, M. Homogenization of inelastic solid materials at finite strains based on incrementalminimization principles. Application to the texture analysis of polycrystals. Journal of the Mechanics and Physics of Solids 2002,50, 2123–2167.
61. Geers, M.G.; Kouznetsova, V.; Brekelmans, W. Gradient-enhanced computational homogenization for the micro-macro scaletransition. Le Journal de Physique IV 2001, 11,

Pr5–145.
62. Kouznetsova, V.; Geers, M.G.; Brekelmans, W.M. Multi-scale constitutive modelling of heterogeneous materials with a gradient-enhanced computational homogenization scheme. International journal for numerical methods in engineering 2002, 54, 1235–1260.
63. Kouznetsova, V.; Geers, M.G.; Brekelmans, W. Multi-scale second-order computational homogenization of multi-phase materials: a nested finite element solution strategy. Computer methods in applied Mechanics and Engineering 2004, 193, 5525–5550.
64. Otero, F.; Oller, S.; Martinez, X.; Salomón, O. Numerical homogenization for composite materials analysis. Comparison with othermicro mechanical formulations. Composite Structures 2015, 122, 405–416. https://doi.org/https://doi.org/10.1016/j.compstruct.2014.11.041.
65. Abaqus v. 6.14 user subroutines reference guide, Dassault Systemes Simulia Corporation.
66. Kanit, T.; Forest, S.; Galliet, I.; Mounoury, V.; Jeulin, D. Determination of the size of the representative volume element for randomcomposites: statistical and numerical approach. International Journal of solids and structures 2003, 40, 3647–3679.
67. Sab, K. On the homogenization and the simulation of random materials. European Journal of Mechanics A-solids 1992, 11, 585–607.
68. Vignoli, L.L.; Savi, M.A. Multiscale Failure Analysis of Cylindrical Composite Pressure Vessel: A Parametric Study. Latin AmericanJournal of Solids and Structures 2018, 15. https://doi.org/10.1590/1679-78254323.
69. Hashin, Z. Theory of mechanical behavior of heterogeneous media 1963.
70. Li, X., Xue, Y., Zhang, D. et al. Robust silicone rubber with high transparency by loading with porous hollow glass microsphere. J Polym Res 30, 426, 2023. https://doi.org/10.1007/s10965-023-03747-x